Inrush Current Mitigation for Grid-Forming Inverters in Islanded Microgrids

Mehmetcan Gursoy
Department of Electrical and Computer Engineering
Kansas State University
Manhattan, KS, USA
gursoy@ksu.edu

Behrooz Mirafzal
Department of Electrical and Computer Engineering
Kansas State University
Manhattan, KS, USA
mirafzal@ksu.edu

Abstract— **Virtual-inertia and droop control methods are commonly used for grid-forming inverters. While the virtual inertia is used to emulate the equation of motion/frequency, if the inverter output voltage is emulated as in synchronous generators, then the method is known as the virtual synchronous generator. An inductive pulse-load, e.g., a relatively large induction motor, connection to a microgrid fed only by grid-forming inverters may lead to blackout due to high inrush currents. This article presents virtual reactance techniques to mitigate the inrush current effects and enhance the inverter's robustness for the safe connection of inductive and dynamic loads. This article also compares the virtual inertia and droop control methods under switching inductive-dynamic loads while the proposed techniques are implemented. Experimental tests are performed considering the linear and nonlinear virtual reactance techniques, and the findings are discussed. The mitigation significantly suppresses the inrush currents while the inverters can perform a normal operation. Furthermore, the frequency and power response of the virtual inertia control with different inertia settings to a sudden change in the load is analyzed. The virtual reactance technique is tested in a laboratory-scale hardware setup of a 208V microgrid fed by 5kVA and 10kVA inverters, and the results are presented in this article.**

Index Terms— **Decentralized control, droop control, grid-forming inverter, inductive-dynamic pulse-load, inrush current, virtual inertia, virtual reactance.**

I. INTRODUCTION

Grid-forming inverters are expected to become the backbone of the modern power infrastructure as the networked microgrid concept is receiving growing attention. Many countries target to expand renewable energy generation by 2050 [1]. Therefore, more inverter-based distributed generation units, mainly powered by renewable energy sources, such as solar panels or wind turbines, are integrated into the power system. In a grid or microgrid, inverters can be used in grid-supporting mode to provide ancillary services [2]-[3], such as harmonics and negative-sequence compensations, voltage and frequency regulation, and enhancing grid stability [4]-[6]. In a networked microgrid, inverters may operate in grid-following or grid-forming modes [7], [8]. On the other hand, the inverters can be programmed to operate autonomously as the primary power source in grid-forming mode [9]-[12]. This mode allows the inverters to operate as a voltage source, generate the amplitude and frequency of the system voltage at the point-of-common-coupling (PCC) for islanded systems, and regulate them at the nominal values. Black-start capability is required to power an islanded subdivision, i.e., a microgrid, after a blackout due to a natural disaster or cyberattack [13]. If the voltage and frequency deviate from the nominal values, grid-forming inverters can perform voltage and frequency restoration [12], [14]. Dynamic and inductive loads may lead to undesired inverter trips that need more investigations on grid-forming strategies.

In islanded microgrids, (re)connection of inverters must be seamless to prevent voltage and current oscillations and maintain the supply/demand balance. An inverter may need to operate in grid-following or grid-forming mode [15]-[18]. In an islanded microgrid, incoming inverters can stay in grid-forming mode or change their mode of operation from zero power-injection grid-following to grid-forming during a synchronization process [10], [12]. Power-sharing strategy during and after the syncing is crucial for stable operation.

There are numerous strategies developed in the literature for controlling the grid-forming inverters. The inverters can be coordinated using a supervisory control structure or decentralized controllers. Nevertheless, a level of communication may require for optimal and economic load dispatching between the inverters [19], [20]. The decentralized strategies without a communication requirement can offer plug-and-play compatibility for inverters, whereas economic dispatching may not be feasible. A microgrid with a communication network becomes a cyber-physical system that is vulnerable to man-in-the-middle cyberattacks. In this case, device-level protection along with system-level security is needed to assure a safe and stable operation [21]-[24].

Investigations show that droop-based controllers are one of the most common control methods for power-sharing in decentralized control due to their simplicity [10]-[12]. Considering the zero inertia nature of the inverter-based systems, a basic droop control can make the system vulnerable to pulse loads, resulting in frequency, voltage, or power oscillations that can trip the inverters. However, the droop controllers can be modified to mimic the dynamics of conventional electric machines, such as synchronous machines, and provide inertia virtually to regulate the frequency and balance the power [26]-[28]. Moreover, the virtual oscillator control (VOC) method is a nonlinear decentralized synchronization and control method used for grid-forming inverters [29]. As the trend in control of grid-forming inverters is moving toward decentralized methods, forecasting and real-time measurements from other devices are not accessible to the local controller of an inverter. Therefore, decentralized

---

This material is based upon work supported by the Department of Energy, Office of Energy Efficiency and Renewable Energy (EERE), Solar Energy Technologies Office, under Award Number DE-EE0008767, and National Science Foundation under Award Number ECCS 1920266.

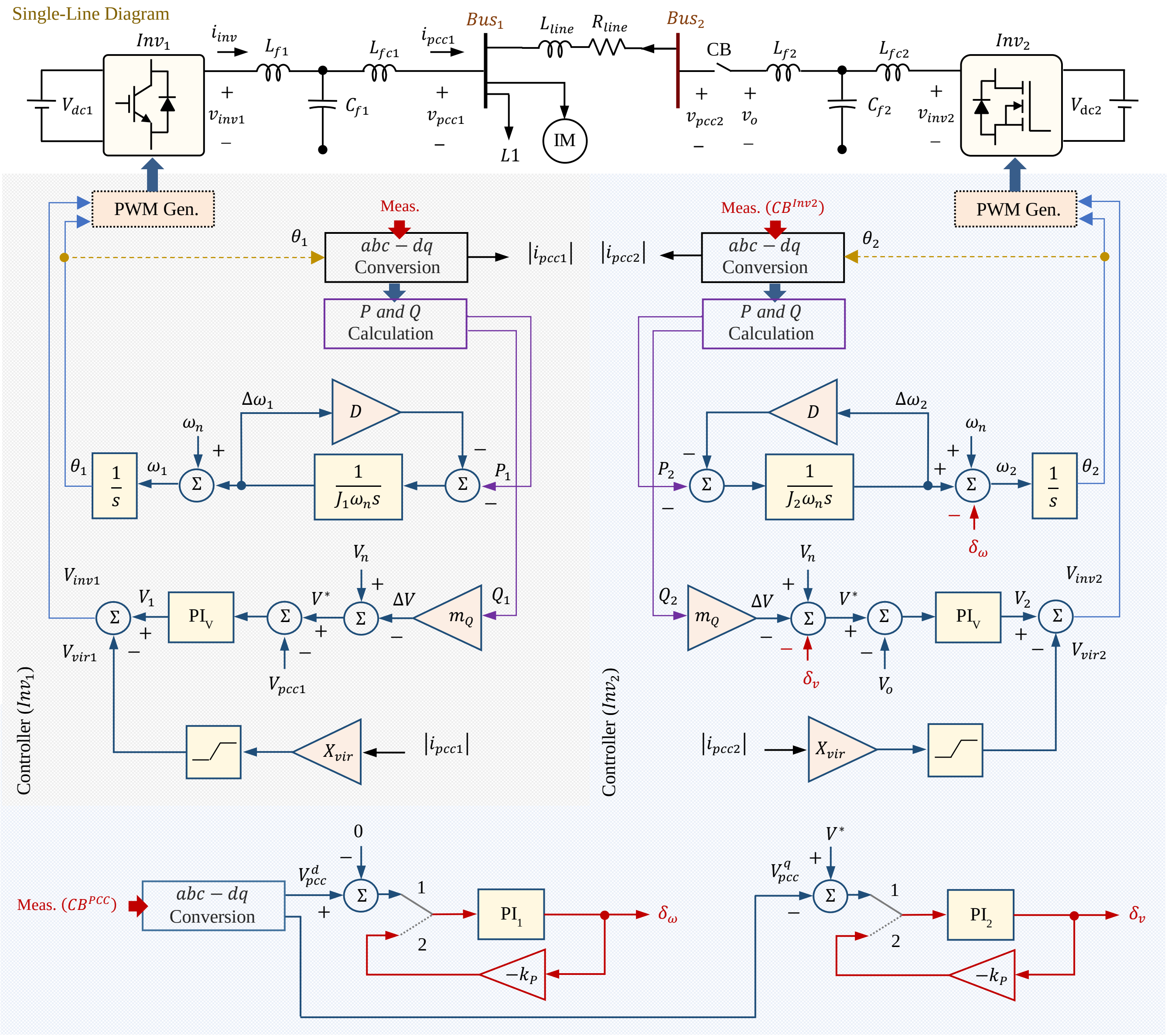

Fig. 1. Single line diagram of the system under study with virtual inertia and reactance are implemented for Inv_1 and Inv_2 to droop control.

inverters might become more sensitive to a power disturbance due to anomalies and sudden dynamic-inductive load changes.

This paper demonstrates the effect of inrush currents caused by inductive-dynamic loads, e.g., an induction motor, in islanded microgrids. The paper presents virtual reactance techniques to mitigate the inrush current and prevent a blackout in the microgrid, fed only by grid-forming inverters. Furthermore, a systematic comparison between droop and virtual inertia control methods for grid-forming inverters is performed while the virtual reactance technique is applied. The performance of the controller and the sensitivity of the system are tested in a hardware setup for different controller parameters and sudden variations in static and dynamic loads. The results depict that the dynamic load can be safely connected to the system by suppressing the inrush currents without tripping the inverters. Faster voltage recovery is observed using the nonlinear mitigation, while less voltage drop is achieved using the linear technique.

In addition to the introduction, the paper contains four more sections. Section II presents the system configuration of the experimental microgrid structure. Section III discusses the details of the droop and virtual inertia controllers. Section IV demonstrates the developed inrush current mitigation techniques. Section V discusses the responses of droop and virtual inertia controls to the inrush currents. Finally, the paper is concluded in Section VI. The discussions are supported by experimental analyses throughout the paper.

II. SYSTEM CONFIGURATION

The single-line diagram of the islanded microgrid structure used in the experiment consisting of two inverters is shown in Fig. 1. In this figure, the virtual inertia control method is used to build PWM reference signals for both inverters. The controller generates the reference signals, i.e., the desired voltage amplitude and frequency, for $V-\omega$ control and load sharing between inverters. In Fig.1, δ_V and δ_ω are used for synchronization of the incoming inverter, i.e., Inv_2. In the

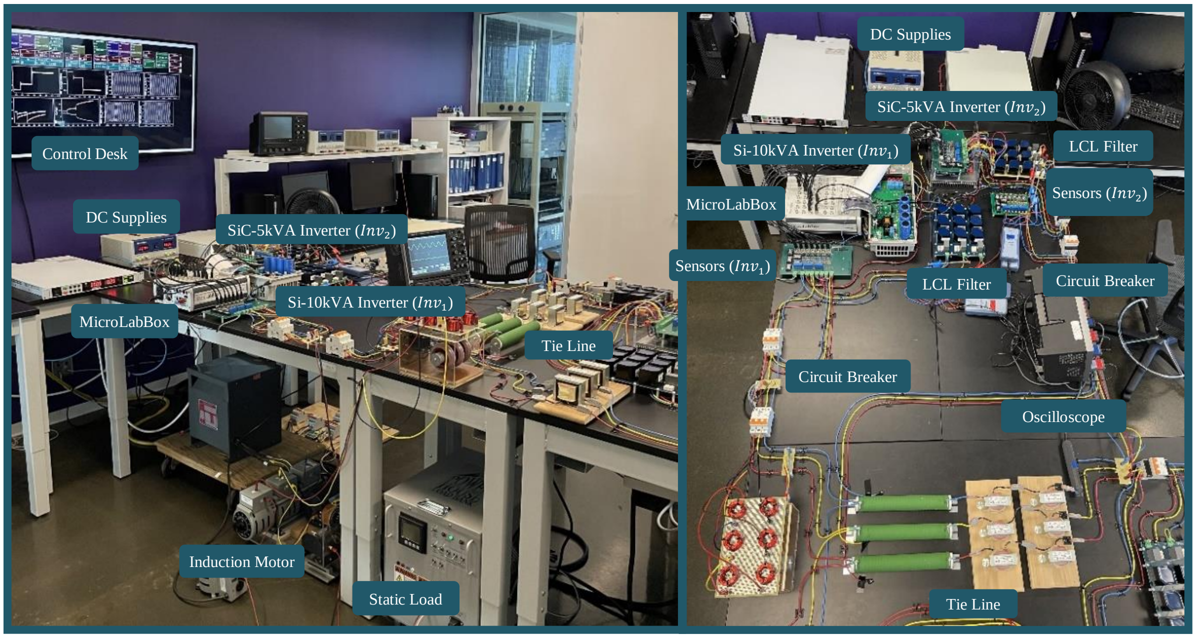

Fig. 2. Experimental islanded microgrid setup used to verify inrush current mitigation techniques and compare the controllers (left), and the top view of the system layout including two inverters (right).

circuit, L_f, L_{fc}, and C_f represent the high-frequency filter inductor, filter coupling inductor, and filter capacitance for each inverter. Notice that the loads, $L1$ and IM are connected to Bus_1. The incoming inverter, Inv_2, is connected to Bus_2 through a circuit breaker (CB). The tie-line impedance is modeled as $R_{line} + jX_{line}$. The details of the controllers for Inv_1 and Inv_2 are in the following sections.

III. THE CONTROL SCHEMES

This paper implements virtual inertia and droop control to compare the performance of the grid-forming inverters during pulse-load events. The control methods are tested in an islanded microgrid hardware setup for comparison purposes, as shown in Fig. 2. The hardware setup includes a three-phase system consisting of $5\,kVA$ SiC-MOSFET and $10\,kVA$ IGBT inverters, two programable DC power supplies, two MicroLabBox controllers (including DSP, A/D, and D/A converters), one $5\,kW$ switched-load, and one three-phase 4-pole $1/3\,hp$ induction motor. In this work, Inv_1 depicts the microgrid which regularly feeds the controllable load, and Inv_2 represents the incoming inverter. The system parameters are in Table I, and the control parameters for each method are provided in Table II. In this study, all data were captured from hardware setup using dSPACE Control Desk software and then plotted using MATLAB software. The test scenarios and associated results are provided for comparison and performance analysis of the presented control strategy.

TABLE I
SYSTEM PARAMETERS

Symbol	Quantity	Value
L_{f1}, L_{f2}	Filter inductances	1 mH
C_{f1}, C_{f2}	Filter capacitances	5 μF (Δ)
R_{cf1}, R_{cf2}	Filter cap. series resistances	1.8 Ω
L_{fc1}, L_{fc2}	Coupling inductances	0.5 mH
L_{line}	Line inductance	5 mH
R_{line}	Line resistance	1 Ω
X_{vir}	Virtual Reactance	5.5 Ω
f_n	Nominal frequency	60 Hz
V_n	Nominal voltage	$208/\sqrt{3}$ V
f_{PWM}	PWM switching frequency	5 kHz
S_{max}	Maximum power rating	1.5 kVA
V_{dc}	DC-bus voltage	350 V

A. Droop Control

The first combination implements droop control for both inverters. The details of the basic droop controller can be found in [10]. For Inv_1, the desired voltage magnitude and frequency are calculated from $V^* = V_n - m_Q Q$ and $\omega^* = \omega_n - m_P P$, where m_P and m_Q are the droop coefficients, and ω_n is the nominal angular frequency, i.e., $60Hz$ in North America. The inverter terminal voltage, v_{inv}, is generated using a PI controller such that the output voltage, v_o, follows V^*. Then,

TABLE II
CONTROL PARAMETERS FOR THE HARDWARE SETUP

Methods	Controller Parameters	Gains
δ_ω, δ_V	PI$_1$, PI$_2$	$k_p = 0.02$, $k_I = 0.25$
Droop Control	PI$_V$	$k_p = 0.0005$, $k_I = 0.2$
	Droop ($P - \omega$)	$m_P = 0.00075$
	Droop ($Q - V$)	$m_Q = 0.001$
	Reset	$k_p = 0.8$
Virtual Inertia Control	PI$_V$	$k_p = 0.0005$, $k_I = 0.2$
	Droop ($Q - V$)	$m_Q = 0.001$
	J	2
	D	1333

the reference signal for the SPWM generator is built using $r_a = \left(V_{inv}/(V_{dc}/2)\right)\sin(\theta)$, where θ is calculated by integrating ω^*.

For Inv_2, when the CB is open, $P = 0$ and $Q = 0$ for the incoming inverter, and thus $V^* = V_n$ and $\omega^* = \omega_n$. To avoid sudden changes in the voltage and current waveforms while closing the CB, V^* and ω^* are modified using the adjustment terms, δ_ω and δ_V, controlled by PI$_1$ and PI$_2$ as follows:

$$\omega^* = \omega_n - m_P P_2 - \delta_\omega \tag{1}$$

$$V^* = V_n - m_Q Q_2 - \delta_V \tag{2}$$

After synchronization and (re)connection of Inv_2, the adjustment terms are forced to zero by changing the state switches' position from 1 to 2, as shown in Fig. 1.

B. *Virtual Inertia Control*

Inertia in power generators, e.g., synchronous generators, refers to the kinetic energy stored in the rotor of the machine due to the rotating mass. In case of a disturbance in the system, such as a fault, load, or a setpoint change, the machine can temporarily resolve the power imbalance between the supply and demand, and regulate the frequency [26], [28]. The controller demonstrated in Fig. 1 leverages the dynamic behavior of electric machines by only implementing the inertia to the inverters' controllers virtually. Thus, the inverters can mimic the dynamic behavior of electric machines. The equation of motion can be expressed as:

$$T_m - T_e = J\frac{d\omega_m}{dt} + D_P\omega_m \tag{3}$$

where, T_m is the mechanical torque generated by the turbine, and T_e is the developed electrical torque, J is the moment of inertia, and D_p is the damping coefficient. This equation can be approximately written in terms of input and output power, also known as the swing equation:

$$P^* - P = J\omega_n\frac{d\omega}{dt} + D\omega \tag{4}$$

where, P^* is the setpoint (desired power) and a constant at the steady-state condition, ω_n is the nominal frequency, and D is the damping coefficient. Eq. (4) can be linearized as follows:

$$-\Delta P = J\omega_n\frac{d\Delta\omega}{dt} + D\Delta\omega \tag{5}$$

One can assume that the steady-state power makes the nominal frequency, ω_n. Therefore, $\Delta\omega$ is basically generated by any change in $-P$, and the inverter frequency is obtained from adding the nominal frequency to a frequency change, i.e., $\omega = \omega_n + \Delta\omega$. Thus, (5) can be rewritten in the Laplace domain as follows:

$$\Delta\omega = \frac{-\Delta P}{(J\omega_n s + D)} \tag{6}$$

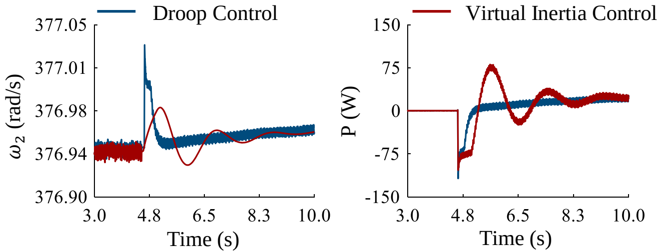

(a) (b)

Fig. 3. Experimental comparison for synchronization dynamics of the incoming inverter using droop control and virtual inertia for both inverters, change in; (a) angular frequency and (b) active power during transients.

Notice that if one assumes $J = 0$, (6) becomes the droop equation, where the droop coefficient $m_p = 1/D$. The damping loop acts like a droop control for power-sharing.

As shown in Fig. 1, Inv_2 is connected to the system after synchronization and closing the circuit breaker. The angular frequency and the output power of Inv_2 for both droop and virtual inertia controls are shown in Fig. 3. The effect of the virtual inertia on ω of Inv_2 can be seen in Fig. 3(a) when the load consumes $70\,W$, shared between two inverters. The performance of inertia control, when $J = 2$, is compared with the droop control. The inertia and damping terms behave like a first-order low pass filter with a gain, $K_\omega = -1/D$, and time constant, $\tau_\omega = J\omega_n/D$. Therefore, it inherently adds delay to $\Delta\omega$ response to a change in active power in comparison with the droop control response. Notice, the selected damping coefficient, $D = 1/m_P = 1333$, corresponds to $m_P = 0.00075$; therefore, ω is same at the steady-state in both test scenarios. The peak of ω using virtual inertia control method is delayed nearly $\tau_{\omega 1} = 2(2\pi 60)/1333 = 0.56\,s$, which filters out the high-frequency oscillations and slows down the inverter response, see Fig. 3(b).

Figs. 4 and 5 show the dynamic responses of the two inverters controlled by virtual inertia method after a step load change in two different scenarios. The initial load is $500\,W$, and then, steped up to $1.5\,kW$ at $t = 1.5\,s$, equally shared between two inverters. For the first scenario, see Fig. 4, $J_1 = 0.04$ and $J_2 = 2$, making Inv_1 faster than Inv_2. In the second scenario, see Fig. 5, Inv_2 becomes faster than Inv_1. In this setup, it should be noted that the load is electrically closer to Inv_1. If one inverter has a higher moment of inertia compared

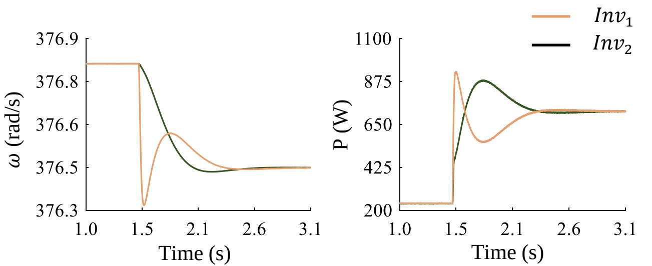

(a) (b)

Fig. 4. Experimentally obtained (a) angular frequency and (b) active power when $J_1 = 0.04$ in Inv_1 and $J_2 = 1$ in Inv_2 after a 1 kW load change.

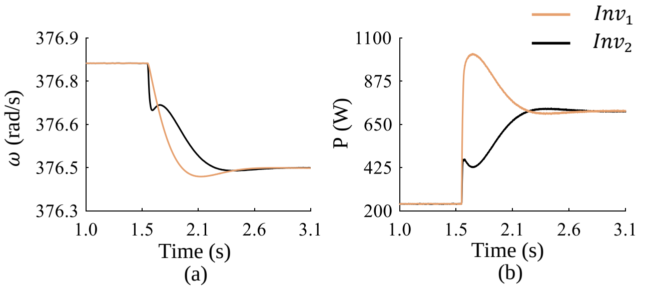

(a) (b)

Fig. 5. Experimentally obtained (a) angular frequency and (b) active power when $J_1 = 1$ in Inv_1 and $J_2 = 0.04$ in Inv_2 after a 1 kW load change.

to the other inverter, a sudden load change can initially result in a larger phase angle for the fastest inverter. This can be clearly seen in the results of the first scenario, see Fig. 4. For the second scenario, Inv_2 is faster than Inv_1; however, Inv_2 is electrically far from the load. Therefore, the ω responses of the two inverters demonstrate almost the same decaying trend. The power dynamics of the two inverters can be explained considering the dynamic responses of θ_1 and θ_2, and the electrical distances (effective impedances) of the inverters with respect to the load. Neglecting the tie-line and filter resistances, from Fig. 1, one can write the power flow from each inverter to the load that is connected to the Bus_1 as follows:

$$P_1 = \frac{V_{inv1} V_{pcc1}}{X_{f1}} sin(\theta_1 - \theta_{pcc1}) \quad (7)$$

$$P_2 = \frac{V_{inv2} V_{pcc1}}{X_{f2} + X_{line}} sin(\theta_2 - \theta_{pcc1}) \quad (8)$$

where, θ_{pcc1} is the voltage angle at Bus_1. Notice in both inverters as the load is stepped up; therefore, $\Delta\omega < 0$. Also, the denominator in (7) is smaller than (8), i.e., $X_{f2} + X_{line} > X_{f1}$, when $X_{f1} = X_{f2}$. Hence, in both scenarios P_1 is initially greater than P_2. Interestingly, in the second scenario, initially $|\Delta\omega_2| > |\Delta\omega_1|$, and since $\theta = \int(\omega_n + \Delta\omega)dt$, then $\theta_1 > \theta_2$. This means that $\theta_1 - \theta_{pcc1} > \theta_2 - \theta_{pcc1}$. Consequently, P_2 in the second scenario has significantly less overshoot compared to the first scenario.

IV. INRUSH CURRENT MITIGATION

Droop and virtual inertia control methods similarly regulate the inverter voltages at their PCCs, see the PI controller, PI_v, in Fig. 1. In this process, the desired voltage, V^*, is obtained from the $Q - V$ droop line in (2) for reactive power-sharing between the inverters. A small m_Q is preferred to ensure less variation in the grid voltage. However, strictly regulating the voltage can lead to inverter trips when an inductive-dynamic load, e.g., an induction motor (IM), is connected to a system fed mainly by inverters. At the start, the rotor of an IM represents a small impedance; therefore, the starting current is typically five to six times the IM's nominal value. In other words, an IM starts as a large electric load (minimal impedance). The IM draws more current from the inverters if the voltage regulation at each inverter terminal is not flexible to reduce the inrush current.

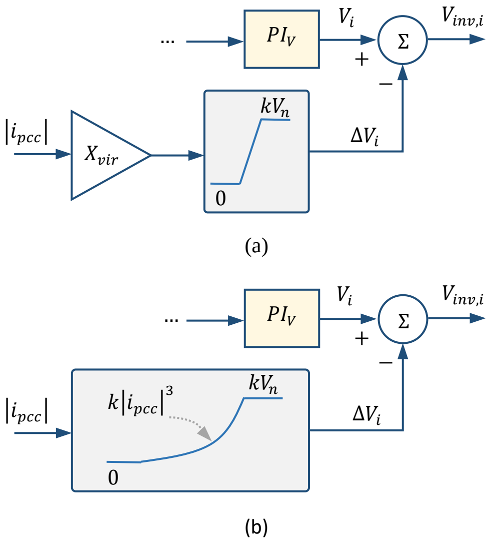

Fig. 6. The mitigation techniques for inrush currents; (a) the linear and (b) nonlinear virtual reactance implementations.

In this work, the voltage control loop is modified using virtual reactance techniques to avoid overcurrent trips. To mitigate the inrush current during an IM start, the controller of grid-forming inverters must allow momentary voltage drops within the IEEE Std. 1547 allowance. To implement the flexibility in adjusting the voltage, the output of PI_v controller of the i^{th} inverter must be quickly adjusted as follows:

$$V_{vir,i} = V_i - \Delta V_i \quad (9)$$

where, ΔV_i is function of the inverter output current. For example, one can write,

$$\Delta V_i = X_{vir} \, |i_{pcc}| \quad (10)$$

where, i_{pcc} is the current drawn from the i^{th} inverter. Notice, the current can expressed in the dq reference frame, and the virtual reactance, X_{vir}, can be defined as $X_{q,vir}$ and $X_{d,vir}$ components for fine mitigating the i_q and i_d current components. Thus, (10) can be rewritten as

$$\Delta V_i = \sqrt{\left(X_{q,vir} \, i_q\right)^2 + \left(X_{d,vir} \, i_d\right)^2} \quad (11)$$

The inrush current mitigation can be achieved linearly using a constant virtual reactance or nonlinearly as a function of the inverter output current. In Fig. 6(a) and 6(b), the linear and nonlinear techniques used in this paper are shown, respectively. The constant, $0 < k < 1$, should be selected based on the system requirements. A k near 1 allows more voltage drop to suppress the effect of inrush and fault currents. Compared to the technique in Fig. 6(a), as the rate of change is faster at high currents using the technique in Fig. 6(b), the voltage will be recovered faster once the motor reaches its nominal speed and the inrush current disappears. In both techniques, the voltage drop is considered after the PI controller. Thus, the controller brings V_i back to the desired level.

As a baseline scenario, the dynamic response of only the $5\,kVA$ SiC-MOSFET inverter, Inv_2, is examined when the $10\,kVA$ IGBT inverter, Inv_1, is disconnected from the circuit shown in Fig. 1. The inverter is tested without and with the virtual reactance implementation given in (9) and (10). Both scenarios use the droop control method. The inverter is initially feeding a $250\,W$ load, and then a $1/3\,hp$ induction motor is connected (by closing its circuit breaker) to the inverter through the tie-line, see Fig. 1. The inverter line current and power delivered to the loads are shown in Fig. 7 for both scenarios. Without implementing the virtual reactance path, the inverter is tripped due to the high inrush current drawn by the motor, see Fig. 7(a), because the inverter tries to firmly regulate the voltage around $V_n = 208\,V$. Notice, the maximum rating of Inv_1 is 5 kVA, which means $\sqrt{2} i_{pcc} = \sqrt{2} S_{max}/\sqrt{3}(208) = 19.63\,A$. However, nearly 30 A peak current flow is observed during the transients, tripping the inverter immediately after connecting the motor. When virtual reactance is added to the voltage control loop with the selected inductance, $L_{vir} = 14.6\,mH$, current spikes are perfectly limited, and the system can operate normally. With implementing the virtual reactance path, the maximum peak current is observed as $11.17\ A$ from Fig. 7(b), within the inverter's maximum capacity. Consequently, P reached the steady-state with ~8% overshoot. The results verify that the inrush current can be mitigated simply using the virtual reactance technique, and the induction motor can be safely started. Further analyses on the linear and nonlinear mitigation techniques, see Fig. 6, using two inverters controlled by droop or virtual inertia are presented in the following section.

V. DROOP & VIRTUAL INERTIA AND LINEAR & NONLINEAR VIRTUAL REACTANCE RESPONSES TO INRUSH CURRENTS

The performance of the inrush current mitigation using linear and nonlinear techniques is examined in this section. Initially, both inverters equally feed a static load of $1\ kW$, and then the $1/3\ hp$ motor is connected to the system, see Fig.1.

Fig. (8) shows the PCC voltages of the two inverters when both are controlled by a basic droop control method but using linear and nonlinear virtual reactance techniques in two different cases. In Fig. 8(b) and 8(a), V_{pcc1} and V_{pcc2} are shown, respectively. The minimum line-to-line voltage is observed at $172.1\ V$ ($\approx 0.83\ V_{p.u.}$) when linear and $167.7\ V$ ($\approx 0.81\ V_{p.u.}$) when nonlinear techniques are used. According to IEEE Std.1547, V_{pcc1} and V_{pcc2} fall in the mandatory operation category. As shown in Fig. 8, the PCC voltage is recovered faster using the nonlinear mitigation technique. At $t = 2.7\ s$, $V_{pcc1} = 205.1\ V$ using the linear mitigation, and $V_{pcc1} = 206.6\ V$ using the nonlinear mitigation.

Fig. (9) shows the PCC voltages of the two inverters when both are controlled by the virtual inertia control method, see Fig. 1, but again in two different cases, using linear and nonlinear virtual reactance techniques. The virtual inertias of both inverters are equal, i.e., $J_1 = J_2 = 2$, in this test. The load is closer to Inv_1, therefore the voltage drops of V_{pcc1} is more than that for V_{pcc2}. A comparison between the voltage transients in Fig. (8) and Fig. (9) reveals that the virtual inertia control method for Inv_1 reacts severely to the IM when starting.

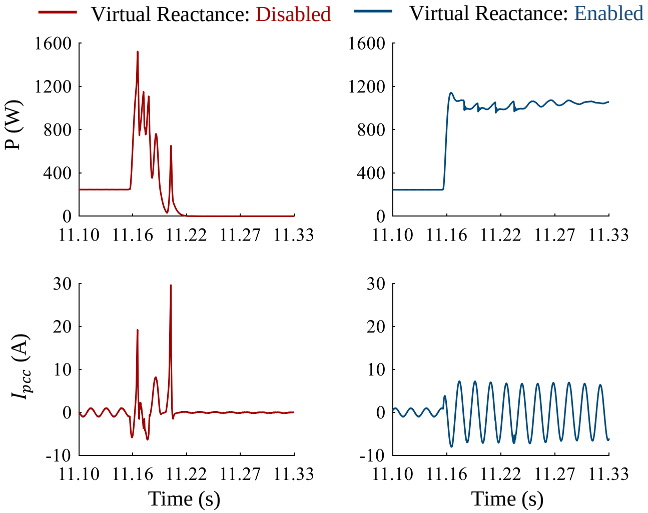

Fig. 7. Experimental obtained output power and current of one inverter when an IM is connected to the system; (a) without the linear virtual reactance, and (b) with the linear virtual reactance implementations.

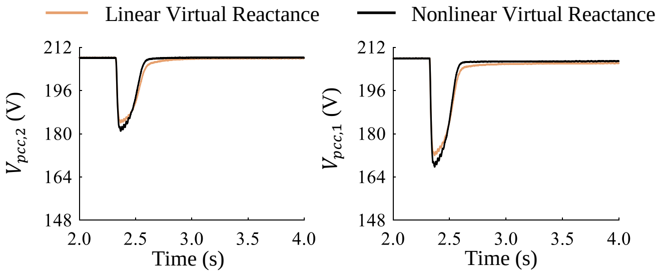

(a) (b)

Fig. 8. Voltage drop observed in the experimental setup using the droop control and linear and nonlinear virtual reactance method techniques.

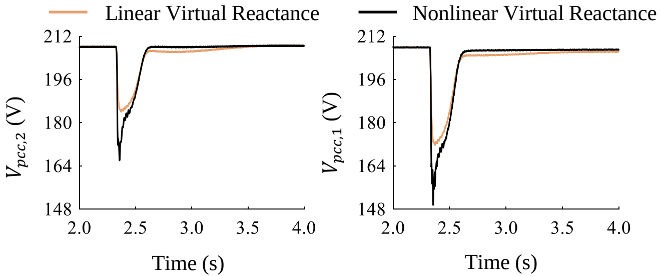

(a) (b)

Fig. 9. Voltage drop observed in the experimental setup using virtual inertia and linear and nonlinear virtual reactance method techniques.

The ω and P responses of both inverters after connecting the IM, when the droop control is implemented with linear and nonlinear inrush current mitigation techniques, are shown in Figs. 10 and 11. A comparison between the transients in Fig. (10) and Fig. (11) for both ω and P responses, reveals that the nonlinear virtual reactance has better performance than the linear one.

The ω and P responses of both inverters after connecting the IM, when the virtual inertia method, see Fig. 1, is implemented with linear and nonlinear inrush current mitigation techniques, are shown in Figs. 12 and 13. A comparison between the transients in Fig. (12) and Fig. (13) for P responses, reveals that

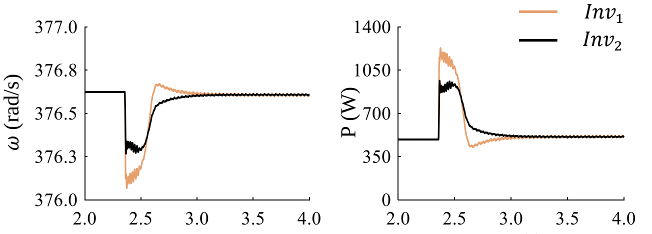

(a) (b)

Fig. 10. Experimentally obtained frequency and active power for both inverters controlled by the droop and the linear virtual reactance strategy.

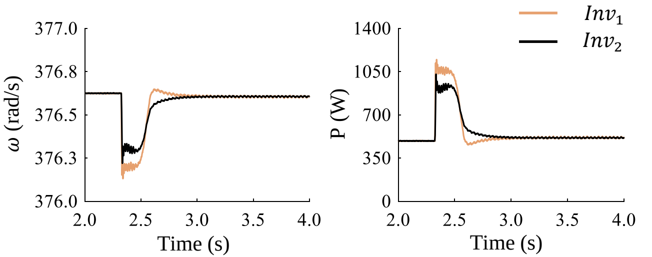

(a) (b)

Fig. 11. Experimentally obtained frequency and active power for both inverters controlled by the droop and the nonlinear virtual reactance strategy.

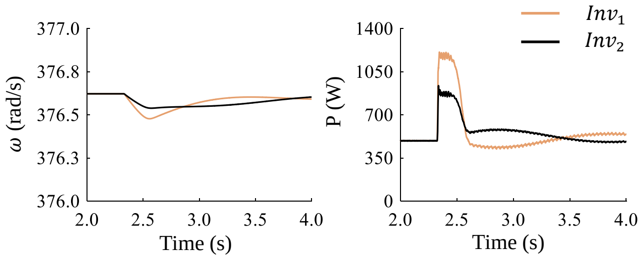

(a) (b)

Fig. 12. Experimentally obtained frequency and active power for both inverters controlled by the virtual inertia and the linear virtual reactance strategy.

the nonlinear virtual reactance technique interacting with the virtual inertia method leads to high-frequency power transients. However, the dynamic of ω damps faster when both inverters controlled by the virtual inertia and the nonlinear virtual reactance strategy.

VI. CONCLUSION

This efficacy of the virtual reactance technique has been experimentally verified for mitigating inrush currents caued by inductive-dynamic loads in an islanded microgrid supplied by grid-forming inverters in this paper. The virtual reactance technique has been implemented for grid-forming inverters controlled by virtual inertia and droop control methods. Moreover, the implementation of linear and nonlinear virtual reactances has been introduced and tested. Both inrush current mitigation techniques successfully prevented undesired inverter trips after connecting an induction motor to the microgrid. The nonlinear technique demonstrated a better transient response for the inverter frequency. The combination of virtual inertia and nonlinear virtual reactance strategies demonstrated the most robust performance of controlling the frequency, but with more high-frequency power transients. More examinations on an optimal nonlinear function for implementing the virtual reactance technique while inverters controlled by virtual inertia method might be needed in the future investigations.

VII. REFERENCES

[1] H. Holttinen *et al.*, "System impact studies for near 100% renewable energy systems dominated by inverter based variable generation," *IEEE Trans. Power Syst.*, vol. 37, no. 4, pp. 3249–3258, 2022.

[2] A. Adib, J. Lamb and B. Mirafzal, "Ancillary services via VSIs in microgrids with maximum DC-bus voltage utilization," *IEEE Trans. Ind. Appl.*, vol. 55, no. 1, pp. 648-658, Jan.-Feb. 2019.

[3] J. Lamb, B. Mirafzal, and F. Blaabjerg, "PWM common mode reference generation for maximizing the linear modulation region of CHB converters in islanded microgrids," *IEEE Trans. Ind. Electron.*, vol. 65, no. 7, pp. 5250–5259, 2018.

[4] A. Adib, F. Fateh and B. Mirafzal, "Smart inverter stability enhancement in weak grids using adaptive virtual-inductance," *IEEE Trans. Ind. Appl.*, vol. 57, no. 1, pp. 814-823, Jan.-Feb. 2021.

[5] A. Adib and B. Mirafzal, "Virtual inductance for stable operation of grid-interactive voltage source inverters," *IEEE Trans. Ind. Electron.*, vol. 66, no. 8, pp. 6002-6011, Aug. 2019.

[6] B. Mirafzal and A. Adib, "On grid-interactive smart inverters: features and advancements," *IEEE Access*, vol. 8, pp. 160526-160536, 2020.

[7] J. Benzaquen *et al.*, "Collaborative Autonomous Grid-Connected Inverters: Flexible grid-forming inverter control for the future grid," *IEEE Electrific. Mag.*, vol. 10, no. 1, pp. 22–29, 2022.

[8] M. S. Pilehvar, D. Sharma, and B. Mirafzal, "Forming interphase microgrids in distribution systems using cooperative inverters," *CCPS Trans, Power Electron. Appl.*, vol. 7, no. 2, June 2022.

[9] M. Lu, S. Dhople, and B. Johnson, "Benchmarking nonlinear oscillators for grid-forming inverter control," *IEEE Trans. Power Electrons.*, vol. 37, no. 9, pp. 10250-10266, Sep. 2022.

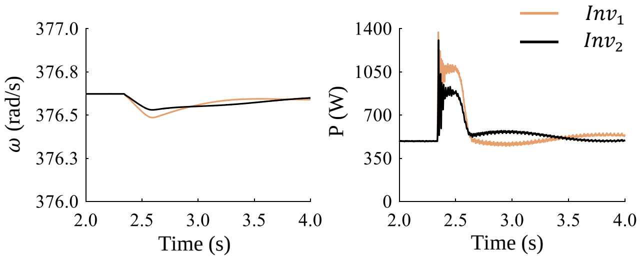

(a) (b)

Fig. 13. Experimentally obtained frequency and active power for both inverters controlled by the virtual inertia and the nonlinear virtual reactance strategy.

[10] D. Sharma, F. Sadeque and B. Mirafzal, "Synchronization of inverters in grid forming mode," *IEEE Access*, vol. 10, pp. 41341-41351, 2022.

[11] R. H. Lasseter, Z. Chen and D. Pattabiraman, "Grid-forming inverters: A critical asset for the power grid," *IEEE J. Emerg. Sel. Topics Power Electron.*, vol. 8, no. 2, pp. 925-935, June 2020.

[12] F. Sadeque and B. Mirafzal, "Frequency restoration of grid-forming inverters in pulse load and plug-in events," *IEEE J. Emerg. Sel. Top. Ind. Electron.*, Early Access, 2022, doi: 10.1109/JESTIE.2022.3186156.

[13] F. Sadeque, D. Sharma, and B. Mirafzal, "Multiple grid-forming inverters in black-start: The challenges," in *2021 IEEE 22nd Workshop on Control and Modelling of Power Electronics (COMPEL)*, 2021, pp. 1–6.

[14] M. Chen, X. Xiao, and J. M. Guerrero, "Secondary restoration control of islanded microgrids with a decentralized event-triggered strategy," *IEEE Trans. Ind. Inform.*, vol. 14, no. 9, pp. 3870–3880, 2018.

[15] M. Kwon *et al.*, "Unified control scheme of grid-connected inverters for autonomous and smooth transfer to stand-alone mode," *IEEE Trans. Power Electron.*, vol. 37, no. 1, pp. 416–425, 2022.

[16] M. Ganjian-Aboukheili *et al.*, "Seamless transition of microgrids operation from grid-connected to islanded mode," *IEEE Trans. Smart Grid*, vol. 11, no. 3, pp. 2106–2114, 2020.

[17] D. S. Ochs, B. Mirafzal, and P. Sotoodeh, "A method of seamless transitions between grid-tied and stand-alone modes of operation for utility-interactive three-phase inverters," *IEEE Trans. Ind. Appl.*, vol. 50, no. 3, pp. 1934–1941, 2014.

[18] M. S. Pilehvar and B. Mirafzal, "Smart inverters for seamless reconnection of isolated residential microgrids to utility grid," in *2020 IEEE Electric Power and Energy Conference (EPEC)*, 2020, pp. 1–6.

[19] Z. Li *et al.*, "Fully distributed hierarchical control of parallel grid-supporting inverters in islanded AC microgrids," *IEEE Trans. Ind. Inform.*, vol. 14, no. 2, pp. 679–690, 2018.

[20] A. Bidram *et al.*, "Resilient and Cybersecure Distributed Control of Inverter-Based Islanded Microgrids," *IEEE Trans. Ind. Inform.*, vol. 16, no. 6, pp. 3881–3894, 2020.

[21] M. Gursoy and B. Mirafzal, "On self-security of grid-interactive smart inverters," *IEEE Kansas Power and Energy Con. (KPEC)*, 2021, pp. 1-6.

[22] M. Gursoy and B. Mirafzal, "Self-security for grid-interactive smart inverters using steady-state reference model," *IEEE 22nd Workshop on Control and Modelling of Power Electronics (COMPEL)*, 2021, pp. 1–5.

[23] T. Hossen, M. Gursoy, and B. Mirafzal, "Digital twin for self-security of smart inverters," in *2021 IEEE Energy Conversion Congress and Exposition (ECCE)*, 2021, pp. 713–718.

[24] T. Hossen, F. Sadeque, M. Gursoy, and B. Mirafzal, "Self-secure inverters against malicious setpoints," in *2020 IEEE Electric Power and Energy Conference (EPEC)*, 2020, pp. 1–6.

[25] X. Xiong *et al.*, "Transient damping method for improving the synchronization stability of virtual synchronous generators," *IEEE Trans. Power Electron.*, vol. 36, no. 7, pp. 7820–7831, 2021.

[26] J. Liu, Y. Miura, and T. Ise, "Comparison of dynamic characteristics between virtual synchronous generator and droop control in inverter-based distributed generators," *IEEE Trans. Power Electron.*, vol. 31, no. 5, pp. 3600–3611, 2016.

[27] B. Long *et al.*, "MPC-controlled virtual synchronous generator to enhance frequency and voltage dynamic performance in islanded microgrids," *IEEE Trans. Smart Grid*, vol. 12, no. 2, pp. 953–964, 2021.

[28] Q. Hu *et al.*, "Grid-forming inverter enabled virtual power plants with inertia support capability," *IEEE Trans. Smart Grid*, pp. 1–1, 2022.

[29] M. Lu, S. Dhople, and B. Johnson, "Benchmarking nonlinear oscillators for grid-forming inverter control," *IEEE Trans. Power Electron.*, vol. 37, no. 9, pp. 10250–10266, 2022.